The Significance of Electrostatic Effects in Phospho-Ester Hydrolysis†

Philip Tole and Carmay Lim*

Contribution from the Departments of Molecular and Medical Genetics, Chemistry, and Biochemistry, University of Toronto, 1 King's College Circle, Toronto, Ontario M5S 1A8, Canada

Received August 25, 1993. Revised Manuscript Received December 6, 1993®

Abstract: The detailed activation free energy profiles for alkaline hydrolysis of the methyl aminoethylenephosphonate (MNP) in vacuum and the changes upon solvation have been computed. The calculations predict that alkaline hydrolysis of MNP in solution proceeds via $(OH)^-$ attack opposite the ring oxygen instead of the nitrogen, in agreement with the concept of apicophilicity. The MNP + $(OH)^-$ solution reaction is predicted to yield a mixture of products, viz., inversion of configuration production from P–O endocyclic cleavage and retention of configuration products from P–O exocyclic cleavage and P–N endocyclic cleavage. Intramolecular charge–charge interactions between the hydroxyl and/or amide protons with neighboring atoms influence the position of the ring nitrogen relative to the ring oxygen in a TBP and facilitate endo- and exocyclic cleavage. There is no evidence of transition-state stereoelectronic effects controlling the MNP + $(OH)^-$ reaction pathway.

1. Introduction

Phosphate esters and anhydrides dominate the chemistry of life processes and are of great chemical, technical, and biological importance.[1] In particular, due to the significance of cyclic five-membered phospho-esters as intermediates in the hydrolysis of ribonucleic acids,[2] there have been numerous experimental studies[3,4] on the hydrolysis of this type of ester. From these studies a set of guidelines have been developed for predicting the product distribution, hydrolysis rates, and stereochemistry for associative nucleophilic substitution reactions at phosphorus. The pioneering studies by Westheimer and co-workers[3,5,6] have provided indirect evidence for the formation of a trigonal-bipyramidal (TBP) pentacovalent intermediate under certain reaction conditions as well as a set of rules governing the dynamics of TBP intermediates.[7] Pseudorotation of a TBP intermediate can proceed via a Berry mechanism, as illustrated in Scheme 1.

Recently, a detailed theoretical study of the basic hydrolysis of the methyl ethylenephosphate (MEP) has established a number of novel mechanistic principles for phospho-ester reactivity in the absence[8,9] and presence of enzymes.[10] The calculations reveal a new mechanism for the MEP + $(OH)^-$ reaction, where hydroxyl ion attack is concerted with pseudorotation to form a TBP intermediate which undergoes ring opening faster than isomerization and subsequent exocyclic cleavage of the methoxy group. Thus, the calculations predict endocyclic cleavage products with retention of configuration in solution. A key finding was that the rate-determining step in solution was governed by the formation of a long-range distorted TBP transition state rather than endo- or exocyclic cleavage of the pseudorotated TBP intermediate. Another new finding was that ring strain, as manifested by the deviation of the ring O–P–O angle relative to its acyclic counterpart, was relieved in the long-range transition state but was retained in the TBP intermediate.

Scheme 1

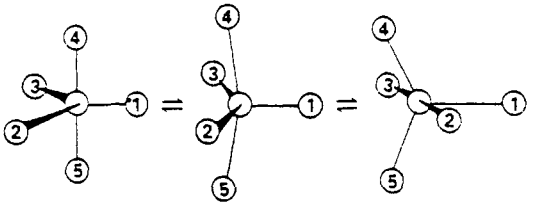

To further establish the factors governing nucleophilic $(OH)^-$ addition to the phosphorus center, a thorough investigation of the basic hydrolysis of the methyl aminoethylenephosphonate (MNP, Figure 1) has been carried out. As the phosphorus center is chiral in MNP, the stereospecificity of the MNP + $(OH)^-$ reaction can be clearly followed. The stereochemical outcome of the various possible pathways for the alkaline hydrolysis of MNP is summarized in Scheme 2. The gas-phase activation free energy profiles (see Method section) for the MNP + $(OH)^-$ reaction were calculated using ab initio molecular orbital methods[11] at the MP2/6-31+G*//HF/3-21+G* level.[12] Solvent effects on the gas-phase activation free energy profiles were estimated using continuum dielectric methods[13,14] to compute the solvation free energies of the reactants, transition states, intermediates, and products. In section 2, the quantum mechanical method and the continuum dielectric method are outlined briefly. Section 3 presents the activation free energy profiles for the MNP + $(OH)^-$ and how they are affected by solvation. The important factors that control the reactivity of MNP with $(OH)^-$ are discussed in section 4, and the results are summarized in section 5. The present work demonstrates that there is an underlying set of unifying

† This work was supported by the Protein Engineering Network Centers of Excellence of Canada.

* Abstract published in *Advance ACS Abstracts,* March 15, 1994.

(1) Westheimer, F. H. *Science* **1987**, *237*, 1173–1178.

(2) Fersht, A. *Enzyme Structure and Mechanism*; W. H. Freeman: New York, 1985.

(3) Westheimer, F. H. *Acc. Chem. Res.* **1968**, *1*, 70–78.

(4) Thatcher, G. R. J.; Kluger, R. *Adv. Phys. Org. Chem.* **1989**, *25*, 99.

(5) Haake, P. C.; Westheimer, F. H. *J. Am. Chem. Soc.* **1961**, *83*, 1102–1109.

(6) Kluger, R.; Covitz, F.; Dennis, E.; Williams, L. D.; Westheimer, F. H. *J. Am. Chem. Soc.* **1969**, *91*, 6066–6072.

(7) Luckenbach, R. *Dynamic Stereochemistry of Pentaco-ordinated Phosphorus and Related Elements*; Georg Thieme Publishers: Stuttgart, 1973.

(8) Lim, C.; Tole, P. *J. Phys. Chem.* **1992**, *96*, 5217–5219.

(9) Tole, P.; Lim, C. In *The Anomeric Effect and Associated Stereoelectronic Effects*; Thatcher, G. R., Ed.; ACS Symposium Series 539; American Chemical Society: Washington, DC, 1993.

(10) Lim, C.; Tole, P. *J. Am. Chem. Soc.* **1992**, *114*, 7245–7252.

(11) Hehre, W. J.; Radom, L.; Schleyer, P. v. R.; Pople, J. A. *Ab Initio Molecular Orbital Theory*; John Wiley and Sons: New York, 1986.

(12) This denotes a single-point energy calculation on the geometry fully optimized at the Hartree–Fock (HF) level with the 3-21+G* basis set using second-order Møller–Plesset perturbation theory (MP2) with a 6-31+G* basis set.

(13) Gilson, M. K.; Honig, B. H. *Proteins: Struct., Funct., Genet.* **1988**, *4*, 7–18.

(14) Lim, C.; Bashford, D.; Karplus, M. *J. Phys. Chem.* **1991**, *95*, 5610–5620.

0002-7863/94/1516-3922$04.50/0

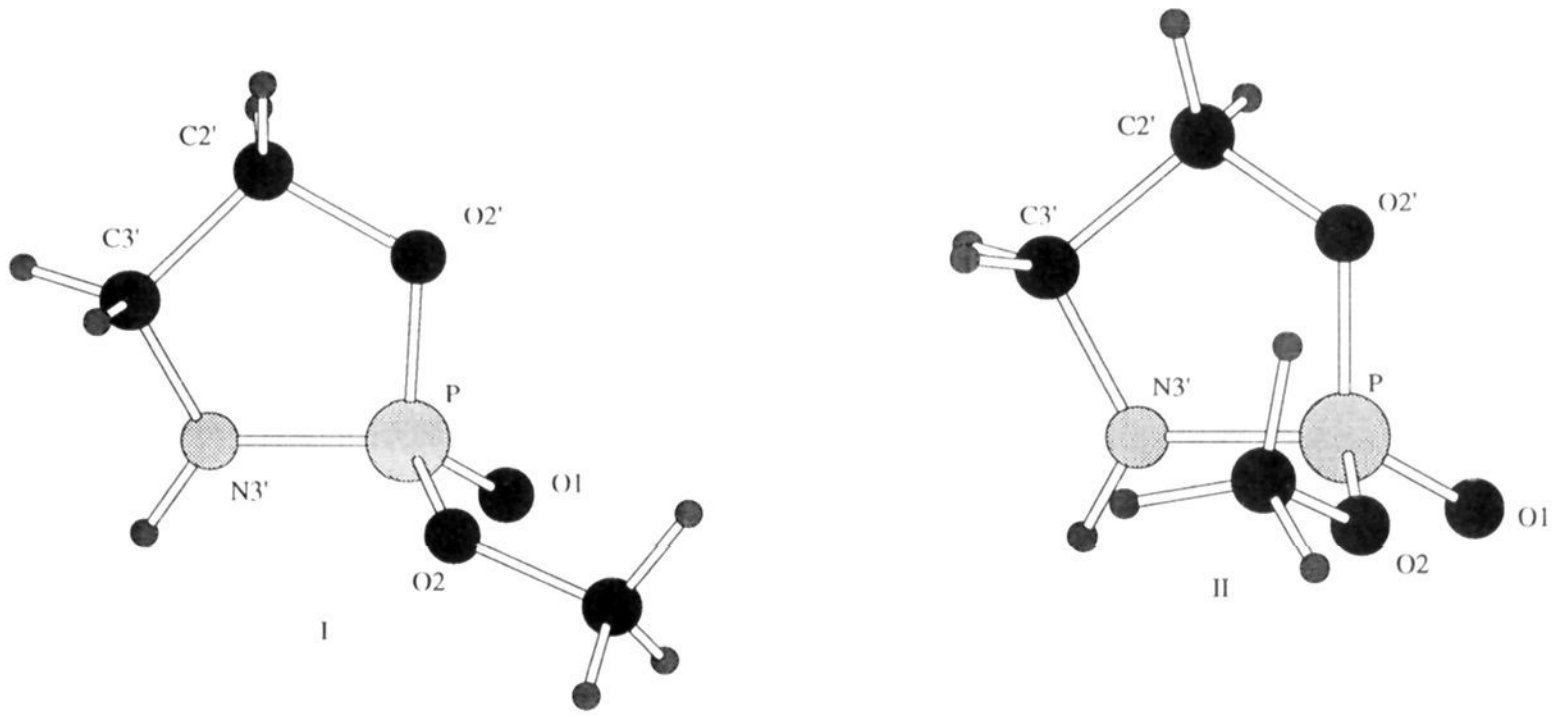

Figure 1. HF/3-21+G* ball and stick geometry of methyl aminoethylenephosphonate energy minims.

Scheme 2

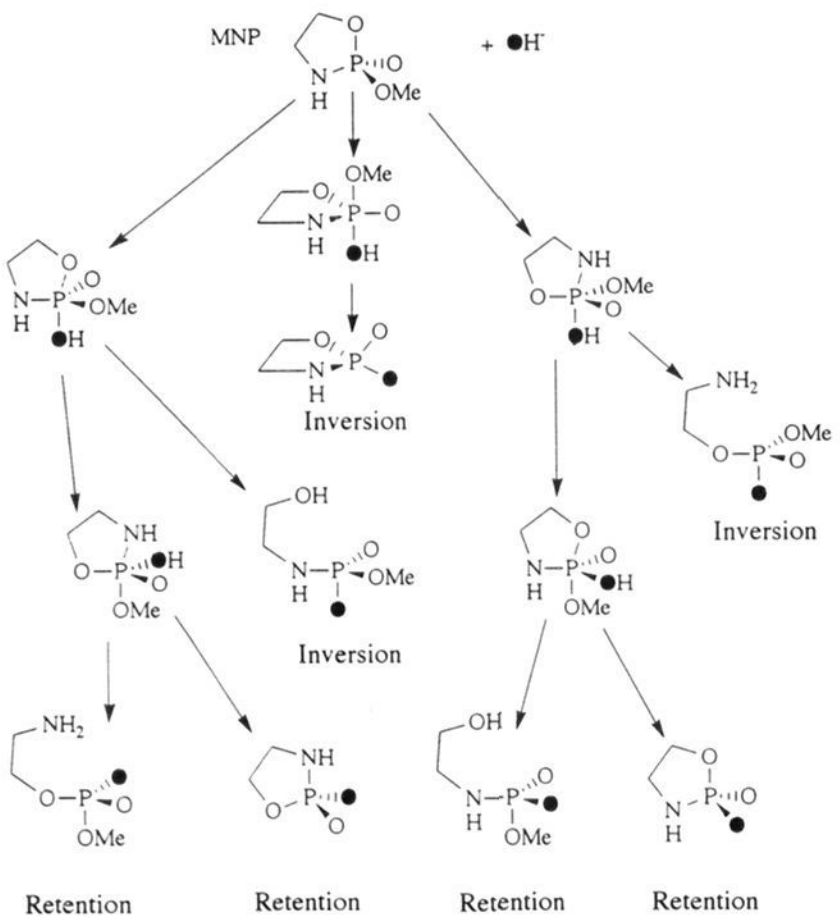

principles, which on one hand reinstates some of the concepts proposed by Westheimer and co-workers[3,4] and on the other hand introduces new key concepts that govern the reactivity of phospho-esters.

2. Method

We briefly outline the methods here and rely on previous work[8,14,15] to provide the details. The ab initio calculations were performed using the program Gaussian 92.[16] The hydroxyl oxygen to phosphorus distance was chosen as the reaction coordinate for the approach of $(OH)^-$ to MNP, and the phosphorus to departing atom distance was chosen as the reaction coordinate for endo- and exocyclic cleavage of the TBP intermediates. Each geometry was fully optimized at the HF/3-21+G* level, and the resulting wave function was used to calculate the electrostatic potential, which was fitted to an atomic point charge model using the program CHELP (charges from electrostatic potentials).[17] A natural bond order (NBO)[18] population analysis was performed. Vibrational frequencies were analyzed in terms of the internal coordinates using the program MOLVIB.[19] From the frequencies and geometries, the vibrational energy (E_{vib}) and entropy (S_{vib}) were calculated according to standard statistical mechanical formulas.[11] The rotational (E_{rot}) and translational (E_{trans}) energy were treated classically. The electronic correlation energy was estimated by second-order Møller–Plesset perturbation theory (MP2) with the 6-31+G* basis for a single point corresponding to the HF/3-21+G* optimized geometry. Addition of the energetic and entropic corrections to the MP2/6-31+G*//HF/3-21+G* [12] activation energies gave the gas-phaes free energy barriers.

The solution free energy barrier, $\Delta A^{\dagger}_{sln}$, from A to B was calculated from a thermodynamic cycle,

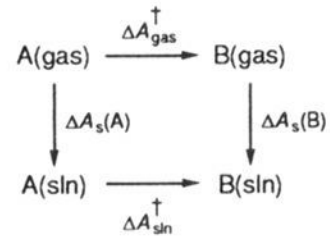

where $\Delta A^{\dagger}_{gas}$ is the gas-phase free energy barrier and the ΔA_s's are solvation free energies; that is

$$\Delta A^{\dagger}_{sln} = \Delta A^{\dagger}_{gas} + \Delta A_s(B) - \Delta A_s(A) \qquad (2.1)$$

The Helmholtz solvation free energy[20] was estimated by solving Poisson's equation using the finite difference method.[13,14] The calculations employed a 71 × 71 × 71 lattice centered on the phosphorus with a grid spacing of 0.25 Å. The low-dielectric region, which was assigned a dielectric constant of 2, was defined as the region inaccessible to contact by a 1.4-Å sphere rolling over a surface defined by the effective solute radii. The latter were taken from the CHARMM version 22[21] van der Waals radii. The HF/3-21+G* geometries and CHELP[17] partial charges, which were assumed to be the same in vacuum and solution, were employed. The difference between the electrostatic potential calculated in solvent and vacuum, characterized by a dielectric constant of 80 and 1, respectively, yielded the solvation free energy.

3. Results

The following nomenclature for the pentacovalent complexes illustrated in Figures 2 and 4 is adopted here, consistent with

(15) Tole, P.; Lim, C. *J. Phys. Chem.* **1993**, *97*, 6212.
(16) Frisch, M. J.; Trucks, G. W.; Head-Gordon, M.; Gill, P. M. W.; Wong, M. W.; Foresman, J. B.; Johnson, B. G.; Schlegel, H. B.; Robb, M.; Replogle, E. S.; Gomperts, R.; Andres, J. L.; Raghavachari, K.; Binkley, J. S.; Gonzalez, C.; Martin, R. L.; Fox, D. J.; Defrees, D. J.; Baker, J.; Stewart, J. J. P.; Pople, J. A. *Gaussian 92*, Revision A; Gaussian Inc.: Pittsburgh, PA 15213, 1992.
(17) Chirlian, L. E.; Francl, M. M. *J. Comput. Chem.* **1987**, *8*, 894.
(18) Reed, A. E.; Curtiss, L. A.; Weinhold, F. *Chem. Rev.* **1988**, *88*, 899.
(19) Kuczera, J.; Kuczera, K. *Program MOLVIB*; Harvard University: Cambridge, 1988.
(20) Chan, S. L.; Lim, C. Bridging continuum dielectric theory, thermodynamics and statistical mechanics. *J. Chem. Phys.*, submitted for publication.
(21) MacKerell, A. D., Jr.; Wiorkiewicz-Kuczera, J.; Karplus, M. All-hydrogen empirical parameterization of nucleic acids for molecular modeling, minimizations and dynamics simulations. Manuscript in preparation.

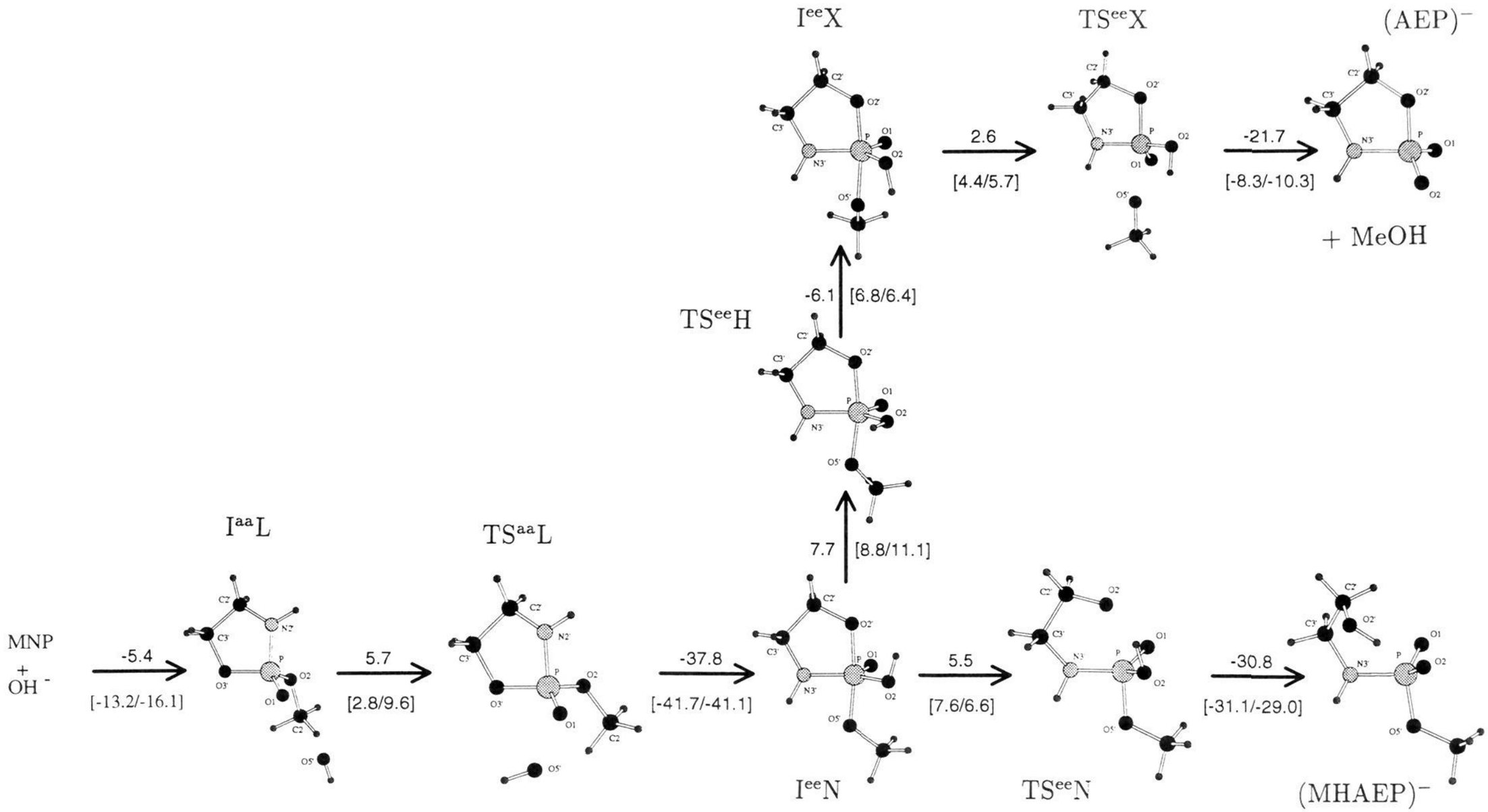

Figure 2. Schematic diagram depicting fully optimized HF/3-21+G* structures for $(OH)^-$ attack opposite the ring nitrogen of MNP in vacuum. The number not enclosed in square brackets denotes the relative free energy (kcal/mol), and [*x*, *y*] denotes [MP2/6-31+G*//HF/3-21+G*, HF/3-21+G*] energies (kcal/mol).

Table 1. Energies, Entropies, and Solvation Free Energies

	E_{HF}[a] (au)	E_{MP2}[b] (au)	E_{TRV}[c] (kcal/mol)	S_{TRV}[d] (cal mol^{-1} K^{-1})	ΔA_s[e] (kcal/mol)
MNP + (OH)$^-$	−809.398 69	−814.890 25	97.168	132.171	−113.17
$I^{aa}L$	−809.424 35	−814.911 36	98.611	110.540	−82.08
$TS^{aa}L$	−809.409 01	−814.906 89	97.935	98.653	−78.24
$I^{ee}N$	−809.474 54	−814.973 31	100.107	92.900	−65.92
$TS^{ee}N$	−809.464 04	−814.961 15	98.613	94.923	−67.58
(MHAEP)$^-$	−809.510 26	−815.010 76	100.499	100.174	−66.42
$TS^{ee}H$	−809.456 87	−814.959 24	98.780	92.397	−68.89
$I^{ee}X$	−809.467 05	−814.970 09	99.927	93.922	−68.02
$TS^{ee}X$	−809.457 92	−814.963 09	98.585	95.454	−64.96
(AEP)$^-$ + MeOH	−809.474 41	−814.976 29	97.795	137.917	−83.42
$I^{ae}L$	−809.458 81	−814.957 16	98.206	99.918	−67.64
$TS^{ae}L$	−809.443 13	−814.944 14	98.392	95.836	−67.87
I^{ae}	−809.464 21	−814.965 39	99.882	93.687	−68.92
$TS^{ae}M$	−809.460 21	−814.960 91	99.159	91.308	−69.41
$I^{ae}N$	−809.467 90	−814.965 51	99.861	94.505	−70.23
$TS^{ae}N$	−809.438 84	−814.937 84	98.109	95.225	−72.25
TSP	−809.439 53	−814.944 87	99.011	90.705	−70.42
$I^{ea}X$	−809.458 03	−814.962 57	99.875	93.716	−65.96
$TS^{ea}X$	−809.437 95	−814.944 42	97.806	96.976	−67.19
$TS^{ea}H$	−809.434 53	−814.942 37	98.244	94.574	−67.91
$TS^{ea}N$	−809.443 91	−814.952 46	98.144	92.659	−62.72

[a] HF energies for fully optimized 3-21+G* geometries. [b] Single-point MP2/6-31+G* energy calculation at 3-21+G* geometry. [c] $E_{TRV} = E_{trans} + E_{rot} + E_{vib}$ in kcal/mol. [d] $S_{TRV} = S_{trans} + S_{rot} + S_{vib}$ in cal mol^{-1} K^{-1}. [e] Solvation free energies in kcal/mol.

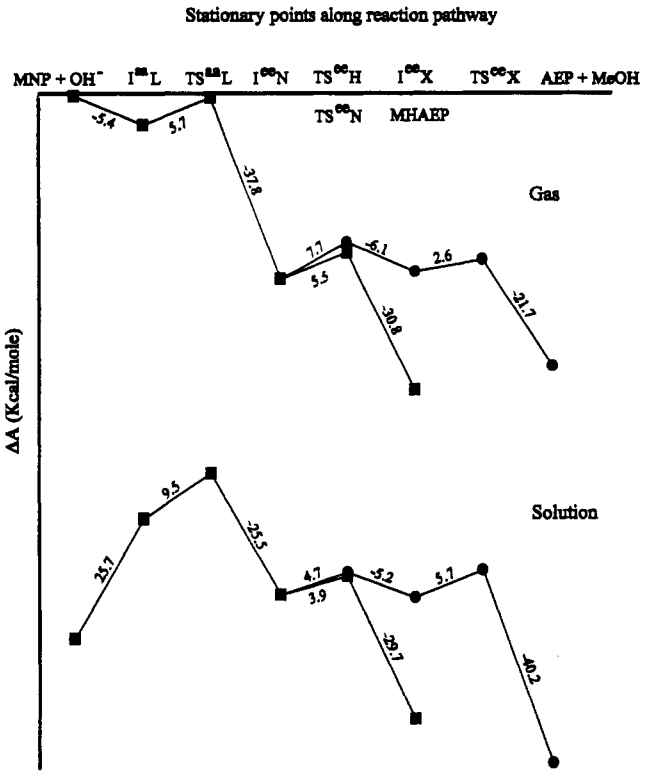

Figure 3. Gas-phase activation *free* energy profile for (OH)$^-$ attack opposite the ring nitrogen of MNP and the change in profile upon solvation. The circles correspond to species on the exocyclic cleavage pathway.

previous work.[15] The letters I and TS denote intermediate and transition state, respectively. The superscripts a and e denote an axial and equatorial position in a TBP, respectively; the first superscript refers to the position of the (OH)$^-$ nucleophile and the second to the NH group location in the TBP. The nonsuperscript letter after I or TS describes the nature of the TBP complex: L for long-ranged ion–dipole complexes, P for pseudorotation, H or M for rotation of the hydroxyl or methoxy group about the P–O(H/Me) bond, N for endocyclic cleavage, and X for exocyclic cleavage. Note that the pseudorotation transition state TSP in Figure 4 was found to be a tetragonal-pyramidal structure with an apical ligand and four basal ligands (see section 3.3.1).

Replacing one of the ring oxygens in MEP with an NH group breaks the symmetry of the ring so that (OH)$^-$ can attack opposite a ring oxygen or nitrogen in MNP. The results for (OH)$^-$ attack opposite MNP(N) will first be discussed, followed by the results for attack opposite MNP(O). Figures 2 and 4 illustrate the gas-phase free energy profiles, and Figures 3 and 5 show how they are altered in solution. The thermodynamic data for the figures are collected in Table 1. The structural information for each of the species is provided as supplementary material in three tables. Unless stated otherwise the values of the atomic charges were obtained from the CHELP program.[17] In the following discussion a frequency for a P–O/P–N bond means that it contains the maximal percentage contribution of a P–O/P–N stretch, but it does not necessary correspond to a pure (100%) P–O/P–N stretch.

3.1. MNP. In vacuum, MNP exists in a gauche and a trans conformation, characterized by a C^{Me}–O–P–O^1 dihedral of 29 and 176°, respectively; the –gauche conformation was found to be unstable. Like MEP, the trans conformer with the methyl group over the ring is less stable than the gauche conformer by 3 kcal/mol at the HF/3-21+G* level (see Figure 1). The energetic and structural data for the lowest energy conformer are employed in the tables and ensuing discussion. The ring N–P–O angle (94.3°) is similar to the ring O–P–O angle (95.1°) in MEP. This suggests that the ethylene bridge and its relative rigidity controls the ring angle about the P atom in a five-membered ring. Replacing a ring oxygen by an NH group does not lead to significant changes in geometry between MEP and MNP except that the P–N bond length is 0.04 Å longer than the P–O^{ring} bond (1.60 Å). The ring forces the nitrogen into a rather flat umbrella-like conformation with the amide proton in the plane of the ring and the single lone pair of electrons out of the ring plane. This and the reduced charge density of a face containing NH (rather than O) are important distinctions between MNP and MEP that result in different reactivity characteristics.

3.2. (OH)$^-$ Attack Opposite MNP(N). 3.2.1. Activation Free Energy Profile in Vacuum for (OH)$^-$ + MNP(N). The gas-phase activation free energy profile for (OH)$^-$ attack opposite the ring nitrogen (Figure 2) is similar to that for (OH)$^-$ attack opposite a ring oxygen in MEP (see Figure 1 in Tole and Lim (1993)[15]). In the ensuing discussion, the structural and thermodynamic results will be presented and compared to the corresponding data for the MEP + (OH)$^-$ pathway.[15]

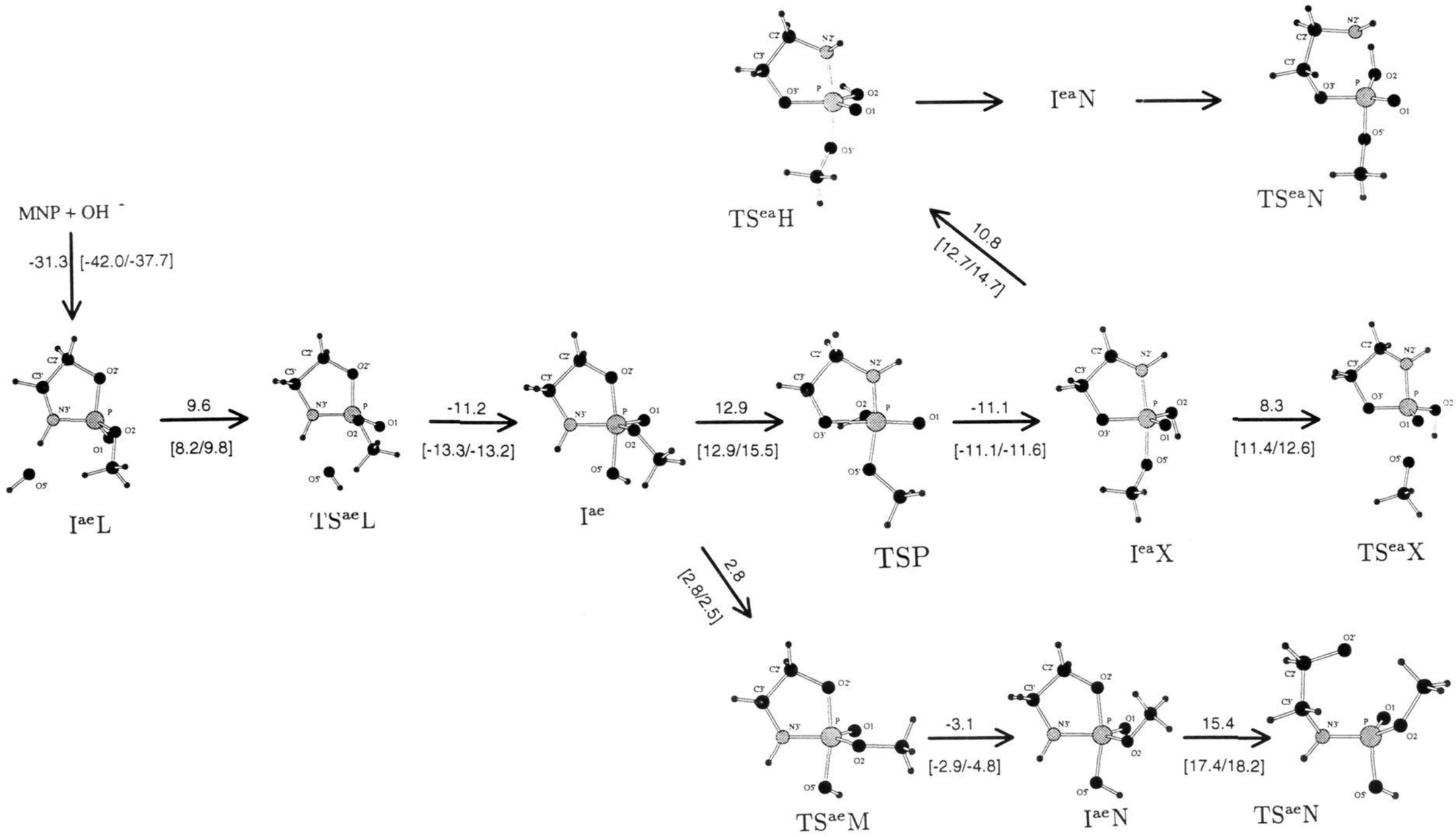

Figure 4. Schematic diagram depicting fully optimized HF/3-21+G* structures for $(OH)^-$ attack opposite the ring oxygen of MNP in vacuum. The number not enclosed in square brackets denotes the relative free energy (kcal/mol), and [*x*, *y*] denotes [MP2/6-31+G*//HF/3-21+G*, HF/3-21+G*] energies (kcal/mol).

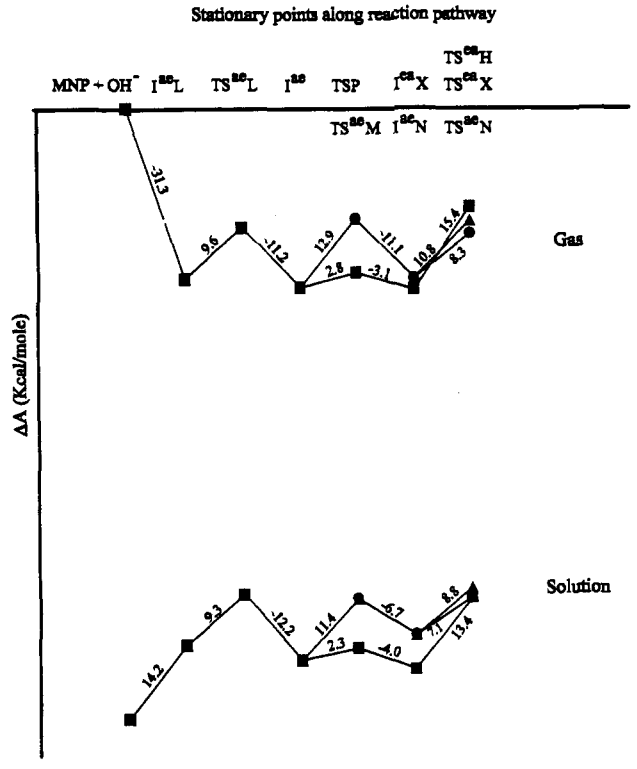

Figure 5. Gas-phase activation *free* energy profile for $(OH)^-$ attack opposite the ring oxygen of MNP and the change in profile upon solvation. The solid circles and triangles correspond to species on the exocyclic and P–N endocyclic cleavage pathways, respectively.

Long-Range Complexes. An ion–dipole minimum ($I^{aa}L$) with a tetrahedral phosphorus (average angle about P = 109°) is found at a P–O^H distance of 5.45 Å (5.35 Å in MEP). As the reaction coordinate decreases to 2.90 Å, a distorted TBP transition state ($TS^{aa}L$) with average N–P–Y, O^H–P–Y, and Y–P–Y (Y = O^1, O^{Me}, $O^{3'}$) angles of 101, 78, and 116°, respectively, is obtained. The long-range complexes are structurally analogous to those found on the MEP + $(OH)^-$ pathway.[15] Thus, the axial ring nitrogen has little geometrical influence in the initial stages of the reaction, which is dictated by steric and charge repulsion between the incoming nucleophile and the three negatively charged atoms O^1, O^{Me}, and $O^{3'}$. However, it has an effect on the $I^{aa}L \rightarrow TS^{aa}L$ gas-phase activation free energy, which is almost double that of the MEP + $(OH)^-$ pathway. This is because an axial ring nitrogen destabilizes $TS^{aa}L$ relative to the corresponding long-range MEP···$(OH)^-$ transition state since oxygen, which forms a more ionic bond with phosphorus as it is more polar than nitrogen, prefers the axial position compared to nitrogen. Evidence for this is provided by the slightly shorter and stronger P–O axial bond (1.65 Å, 803 cm^{-1})[15] in the long-range MEP···$(OH)^-$ transition state relative to the P–N axial bond (1.69 Å, 788 cm^{-1}) in the $TS^{aa}L$ transition state.

Pseudorotation. As in the case of MEP,[8,15] an intermediate with the hydroxyl group axial was found to be unstable since it underwent spontaneous pseudorotation to yield $I^{ee}N$. This is not surprising since the factors that drive pseudorotation in the MEP + $(OH)^-$ pathway[15] are present here, i.e., (i) a very favorable free energy gradient to form an $I^{ee}N$ intermediate with the hydroxyl group equatorial (−38 kcal/mol vs −35 kcal/mol for MEP), (ii) attractive H^O···$O^{3'}$ and repulsive O^H···$O^{3'}$/O^{Me} interactions, which causes lengthening of the P–$O^{3'}$ bond and widening of the $O^{3'}$–P–O^{Me} angle, and (iii) low-frequency ring torsions and lack of steric hindrance. In addition, the reduced polarity of nitrogen compared to oxygen (resulting in an increased covalency of the P–N bond) favors an equatorial nitrogen in a TBP and, thus, pseudorotation.

Table 2. Two-Electron Stabilization Energies from NBO Analysis

species	donor orbital	acceptor orbital	$\Delta E^2_{n\sigma^*}$ (kcal/mol)
$TS^{aa}L$	O^1	P–$O^{3'}$	39.3
	O^{Me}	P–O^H	<0.05
$I^{ee}N$	$O^{2'}$	O–H	2.9
	$O^{5'}$	N–H	1.0
	O^H	P–$O^{2'}$	<0.5
$TS^{ee}N$	$O^{2'}$	O–H	19.1
	O^H	P–$O^{2'}$	<0.5
$TS^{ee}H$	O^H	P–$O^{2'}$	5.2
	O^H	P–$O^{5'}$	3.3
$I^{ee}X$	$O^{5'}$	O–H	2.3
	$O^{5'}$	N–H	<0.5
	O^H	P–$O^{5'}$	0.7
$TS^{ee}X$	$O^{5'}$	O–H	60.9
	$O^{5'}$	N–H	<0.05
	O^H	P–$O^{5'}$	<0.5
$TS^{ae}L$	O^1	P–N	30.7
	O^H	N–H	17.3
	O^{Me}	P–O^H	<0.05
I^{ae}	O^{Me}	P–O^H	1.8
$TS^{ae}M$	O^{Me}	P–O^H	7.7
	O^{Me}	P–$O^{2'}$	6.2
$I^{ae}N$	$O^{2'}$	C^{Me}–H	1.7
	O^{Me}	P–$O^{2'}$	1.4
$TS^{ae}N$	$O^{2'}$	C^{Me}–H	9.9
	O^{Me}	P–$O^{2'}$	<0.5
TSP	O^{ring}	O–H	<0.5
$I^{ea}X$	$O^{5'}$	O–H	3.3
	O^H	P–O^{Me}	<0.5
$TS^{ea}X$	$O^{5'}$	O–H	55.9
	O^H	P–O^{Me}	<0.5
$TS^{ea}H$	O^H	P–O^{Me}	5.8
	O^H	P–N	4.2
$TS^{ea}N$	N	O–H	41.7
	O^H	P–N	<0.5

Isomerization. Isomerization of $I^{ee}N \rightarrow I^{ee}X$ in vacuum occurs via a $TS^{ee}H$ transition state where the hydroxyl hydrogen is cis or trans to O^1. The trans structure (H–O–P–O^1 = −178°) is slightly more stable (by 0.85 kcal/mol at the HF/3-21+G* level) than the cis structure (H–O–P–O^1 = −17°). The gas-phase free energy barrier for isomerization is 1 kcal/mol less than the corresponding barrier along the MEP + $(OH)^-$ pathway. Unlike the endo- and exocyclic cleavage intermediates on the MEP + $(OH)^-$ pathway, which are nearly isoenergetic, $I^{ee}N$ is more stable than $I^{ee}X$ by 2 kcal/mol. This is because in $I^{ee}N$, *both* axial $O^{2'}$ and $O^{5'}$ atoms, which are 2.02 and 2.19 Å from H^O and H^N, respectively, have favorable interactions with the hydroxyl and amide protons (see also Table 2). In contrast, one of the axial atoms does not benefit from any stabilizing interactions with H^O in $I^{ee}X$ and the TBP endo- and exocyclic cleavage intermediates on the MEP + $(OH)^-$ pathway.

Endocyclic vs Exocyclic Cleavage. As in the MEP + $(OH)^-$ pathway,[15] $I^{ee}N$ can either undergo direct P–O endocyclic cleavage or isomerize to yield $I^{ee}X$ and exocyclic cleavage of the methoxy group. However, unlike the MEP + $(OH)^-$ pathway in vacuum, where the free energy barrier for exocyclic cleavage (9.9 kcal/mol) is roughly twice that for ring-opening (4.5 kcal/mol), the reverse is true for the MNP + $(OH)^-$ gas-phase pathway (Figure 2). This reversal results from a slight increase in the ring-opening barrier (5.5 kcal/mol) and a large decrease in the exocyclic cleavage barrier (2.6 kcal/mol). The former results from greater endocyclic cleavage in the $TS^{ee}N$ transition state, as indicated by a P–$O^{2'}$ distance of 2.47 Å compared to 2.24 Å in the corresponding transition state along the MEP + $(OH)^-$ pathway. Although the extent of exocyclic cleavage is similar to that in the MEP + $(OH)^-$ pathway (P–O^{Me} = 2.31 Å), the 7.3 kcal/mol drop in the gas-phase exocyclic cleavage barrier is probably due to the reduced charge repulsion between the departing methoxide and an equatorial amide group relative to an oxygen. Direct ring-opening with inversion of configuration is unlikely, as the transition state

involved is much higher in energy (by 29.3 kcal/mol at the HF/3-21+G* level) than the pseudorotated $TS^{ee}N$ transition state.

3.2.2. Solvent Effects on the Gas-Phase Activation Free Energy Profile for $(OH)^-$ + MNP(N). Figure 3 illustrates the qualitative effects of solvent on the gas-phase activation free energy profile for the $(OH)^-$ + MNP(N) reaction. As in the MEP + $(OH)^-$ pathway,[15] solvation leads to the disappearance of the ion–dipole minimum so that nucleophilic addition of $(OH)^-$ to MNP results in the formation of $I^{ee}N$ with a free energy barrier of 35 kcal/mol in solution. Solvation decreases the P–O^H rotational free energy barrier (by 3 kcal/mol) but increases the exocyclic cleavage barrier (by 3 kcal/mol) so that the latter is slightly greater than the ring-opening barrier (by 2 kcal/mol). Thus, in vacuum and solution, the results show that $(OH)^-$ attack opposite the ring nitrogen in MNP proceeds via a rate-limiting long-range $TS^{aa}L$ transition state to yield both endo- and exocyclic cleavage products with retention of configuration. This is in contrast to the alkaline hydrolysis of MEP,[15] where the free energy barrier for exocyclic cleavage is more than twice that for ring-opening (by >9 kcal/mol) in vacuum and solution; thus, exclusive ring-opening is predicted.

3.3. $(OH)^-$ Attack Opposite the Ring MNP(O). 3.3.1. Activation Free Energy Profile in Vacuum for $(OH)^-$ + MNP(O). Figure 4 summarizes the gas-phase activation free energy profile for $(OH)^-$ attack opposite the ring oxygen of MNP. In the following discussion, the structural and thermodynamic results will be presented and compared to the $(OH)^-$ + MNP(N) pathway as well as the $(OH)^-$ + MEP pathway.

Long-Range Complexes. The approach of $(OH)^-$ opposite the ring oxygen of MNP results in an ion–dipole minimum ($I^{ae}L$) at a P–O^H distance (3.60 Å) that is almost 2 Å shorter than that for $I^{aa}L$. This is because one of the electron lone-pairs on $O^{3'}$ in $I^{aa}L$ has been replaced with an amide proton in the nucleophile pathway in $I^{ae}L$. Thus, there is less charge repulsion in $I^{ae}L$ compared to $I^{aa}L$, so that the gas-phase formation free energy of $I^{ae}L$ is 26 kcal/mol more favorable than that of $I^{aa}L$. Like the $I^{aa}L$ intermediate, the cyclic part of the complex is MNP-like with an average angle about P of 109°, indicating that the phosphorus remains tetrahedral.

The gas-phase activation free energy for $I^{ae}L \rightarrow TS^{ae}L$, where the reaction coordinate decreases from 3.60 to 2.53 Å, is 4 kcal/mol higher than that for $I^{aa}L \rightarrow TS^{aa}L$, where the decrease is greater (5.45 to 2.90 Å). As in the long-range $I^{ae}L$ intermediate, the amide group reduces the charge–charge repulsion in $TS^{ae}L$. Consequently, the $TS^{ae}L$ transition state has a less distorted TBP geometry (the average O^{ring}–P–Y, O^H–P–Y, and Y–P–Y (Y = O^l, O^{Me}, N) angles are 99, 81, and 117°, respectively) and a shorter P–O^H distance than the long-range MEP···$(OH)^-$ or $TS^{aa}L$ transition state. The N–P–O^H angle is 3° smaller than the corresponding angle in the long-range MEP···$(OH)^-$ or $TS^{aa}L$ transition state, probably due to favorable interactions between the hydroxyl oxygen and the amide proton (see Table 2).

Pseudorotation. Attack of $(OH)^-$ opposite the ring oxygen of MNP yields a stable I^{ae} TBP intermediate with the hydroxyl group axial and average $O^{2'}$–P–Y, O^H–P–Y, and Y–P–Y (Y = O^l, O^{Me}, N) angles of 90, 90, and 120°, respectively. Nucleophilic addition of $(OH)^-$ opposite MNP(O) is not concerted with pseudorotation unlike $(OH)^-$ attack opposite the MNP(N) or MEP(O) since some of the factors driving pseudorotation are no longer present. Pseudorotation of $I^{ae} \rightarrow I^{ea}X$ not only requires a gas-phase activation free energy of 12.9 kcal/mol but is thermodynamically unfavorable; the gas-phase free energy difference between I^{ae} and the pseudorotated $I^{ea}X$ intermediate with the hydroxyl group equatorial is positive (1.8 kcal/mol). Spontaneous pseudorotation of I^{ae} may also be hindered by attractive in-plane interactions between the amide proton and

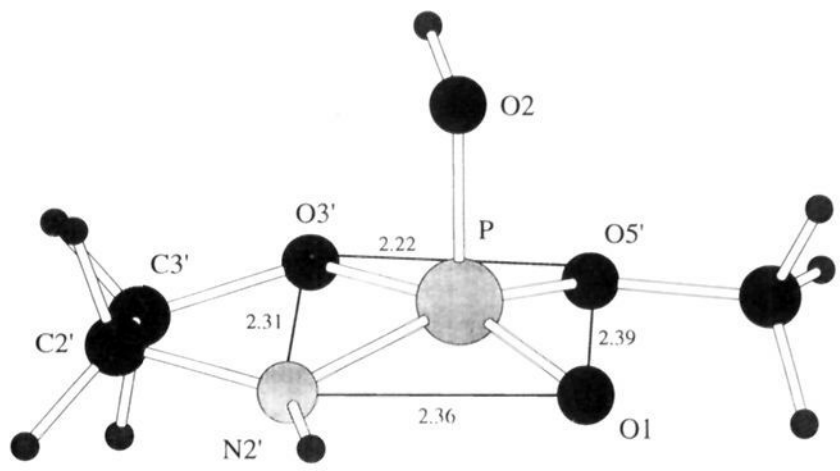

Figure 6. HF/3-21+G* ball and stick geometry of the tetragonal-pyramidal pseudorotation transition state.

the hydroxyl O (H^N–O^H = 2.20 Å, H–N–P–O^H = 0.3°) as well as the hydroxyl H and O^l (H^O–O^l = 2.30 Å, H–O–P–O^l = –2.9°).

To locate the pseudorotation TSP transition state, the O^{ring}–P–O^H angle, which was 167° in I^{ae}, was initially fixed at 140° while the other degrees of freedom were optimized; subsequently, the O^{ring}–P–O^H angle was relaxed and all degrees of freedom were optimized to obtain a saddle point with a single negative frequency. In contrast to the TBP geometry of the I^{ae} and $I^{ea}X$ intermediates, the TSP pseudorotation transition state has a tetragonal-pyramidal geometry with O^l, O^{Me}, O^{ring}, and N forming the square base; the average side length and corner angle of the square are 2.32 Å and 90° (Figure 6). Contraction of the O^{ring}–P–O^H angle from 167° in I^{ae} to 93° and the associated expansion of the O^{ring}–P–O^l and N–P–O^{Me} angles from 99 and 117° in I^{ae} to 160 and 152° in TSP yields the four-membered base (Figure 6). The proximity of the hydroxyl hydrogen to the ring oxygen (H^O–O^{ring} = 2.35 Å, H–O–P–O^{ring} = –27°) causes the P–O^{ring} bond to lengthen slightly (by 0.02 Å relative to I^{ae}), but results in no apparent stabilization of the TSP transition state (see Table 2).

Exocyclic vs Endocyclic Cleavage. The pseudorotated $I^{ea}X$ intermediate is activated for exocyclic cleavage since the hydroxyl hydrogen is 1.99 Å from the methoxy oxygen with a H–O–P–O^{Me} dihedral angle of –8°. The $I^{ea}X$ intermediate and $TS^{ea}X$ transition state have geometries similar to the corresponding species on the MEP + $(OH)^-$ exocyclic cleavage pathway, except that the endocyclic axial bond is 0.04 Å longer. Relative to the corresponding gas-phase MEP + $(OH)^-$ pathway, the substitution of NH for the axial ring oxygen lowers the exocyclic cleavage activation free energy, $I^{ea}X \rightarrow TS^{ea}X$ (by 1.6 kcal/mol), but raises the activation free energy for hydroxyl group rotation, $I^{ea}X \rightarrow TS^{ea}H$ (by 2.1 kcal/mol).

When the hydroxyl group in $I^{ea}X$ is rotated so that it is cis to the equatorial ring oxygen instead of the axial methoxy oxygen, the P–O^{Me} distance decreases from 1.75 Å in $I^{ea}X$ to 1.71 Å in $TS^{ea}H$, whereas the P–N bond length and P–N–C angle increase from 1.77 Å and 114° in $I^{ea}X$ to 1.81 Å and 117° in $TS^{ea}H$. Rotation of the hydroxyl group so that it is cis to the axial nitrogen would further increase the P–N bond length and P–N–C angle. This is supported by the fact that the axial P–$O^{2'}$ bond length in $I^{ee}N$ is 0.06 Å longer than that in $TS^{ee}H$. A similar increase would result in a P–N bond length of 1.87 Å when the O–H bond is cis to the axial P–N bond. The long P–N bond length probably decreases the overlap population between the phosphorus and the nitrogen to an extent such that attempts to locate an $I^{ea}N$ intermediate failed as the ring opened. However, a transition state for P–N endocyclic cleavage ($TS^{ea}N$) was located at a P–N distance of 2.35 Å. This suggests that $I^{ea}N$ exists in a very broad, shallow well and the gas-phase free energy barrier for P–N ring-opening is probably <1 kcal/mol. The latter, in turn, implies that $I^{ea}N$ is less stable than $I^{ea}X$, in contrast to the nearly isoenergetic endo- and exocyclic cleavage intermediates of the MEP + $(OH)^-$ pathway.

Table 3. Relative Thermodynamic Parameters (kcal/mol)

	A → B							
	$TS^{ee}N \rightarrow TS^{ea}N$	$TS^{ee}H \rightarrow TS^{ea}H$	$TS^{ee}X \rightarrow TS^{ea}X$	$I^{ee}X \rightarrow I^{ea}X$	$I^{ee}N \rightarrow I^{ae}N$	$TS^{ee}H \rightarrow TS^{ae}M$	$I^{ee}X \rightarrow I^{ae}$	$TS^{ee}N \rightarrow TS^{ae}N$
ΔE^b	5.0	10.0	10.9	4.6	4.7	−0.7	2.9	14.1
$T\Delta S^c$	−0.7	0.6	0.4	−0.1	0.5	−0.3	−0.1	0.1
$\Delta A_{gas}{}^d$	5.7	9.4	10.5	4.7	4.2	−0.4	3.0	14.0
$\Delta\Delta A_s{}^e$	4.8	1.0	−2.2	2.1	−4.3	−0.5	−0.9	−4.6
$\Delta A_{sln}{}^f$	10.5	10.4	8.3	6.8	−0.1	−0.9	2.1	9.4

[a] For A → B in kcal/mol. [b] $\Delta E = \Delta E_{MP2} + \Delta E_{TRV}$. [c] $T\Delta S = [S_{TRV}(B) - S_{TRV}(A)]\ 298.15^{-3}$. [d] $\Delta A_{gas} = \Delta E - T\Delta S$. [e] $\Delta\Delta A_s = \Delta A_s(B) - \Delta A_s(A)$. [f] $\Delta A_{sln} = \Delta A_{gas} + \Delta\Delta A_s$.

Ring-opening can also occur without pseudorotation by rotating the methoxy group in I^{ae} to yield $I^{ae}N$, which can subsequently undergo P–O^{ring} cleavage. The gas-phase activation free energy for rotation of the methoxy group in $I^{ae} \rightarrow TS^{ae}M$ (2.8 kcal/mol) is 3.3 kcal/mol less than that for rotation of the hydroxyl group in $I^{ee}X \rightarrow TS^{ee}H$ (6.1 kcal/mol). This is not due to stabilization of $TS^{ae}M$ relative to $TS^{ee}H$, as their gas-phase free energies differ by only −0.4 kcal/mol (Table 3). Instead, the decrease in the methoxy group rotational barrier stems from ground-state destabilization of I^{ae} relative to $I^{ee}X$ (ΔA_{gas} = 3.0 kcal/mol, Table 3) since the axial exocyclic oxygen is stabilized by favorable in-plane interactions with H^O in $I^{ee}X$ but not in I^{ae}. Rotation of the methoxy group in $TS^{ae}M$ so that it is cis to an axial P–O bond increases the latter by 0.01–0.02 Å, which is less than the increase (0.04–0.06 Å) caused by the corresponding hydroxyl group rotation in $TS^{ee}H$. The importance of the hydroxyl group in activating endo-/exocyclic cleavage is also manifested in the large difference between the gas-phase P–O endocyclic cleavage barrier of $I^{ae}N$ (15.4 kcal/mol) and $I^{ee}N$ (5.5 kcal/mol) (see also Table 2). Due to the lack of stabilizing interactions between the methyl group and the departing ring oxygen, the $TS^{ae}N$ transition state is located at a longer $P–O^{2'}$ distance (3.08 Å) compared to $TS^{ee}N$ (2.47 Å).

3.3.2. Solvent Effects on the Activation Free Energy Profile for $(OH)^-$ + MNP(O). Figure 5 illustrates the qualitative effects of solvent on the gas-phase activation free energy profile for the $(OH)^-$ + MNP(O) reaction. Solvation again leads to the disappearance of the ion–dipole minimum and induces a solution free energy barrier of 23.5 kcal/mol for MNP + $(OH)^- \rightarrow TS^{ae}L$. Unlike the $I^{aa}L$ and $TS^{aa}L$ long-range complexes, which are better solvated than the $I^{ee}N$ and $I^{ee}X$ intermediates, the solvation free energy of the I^{ae} intermediate is similar to that of the $I^{ae}L$ and $TS^{ae}L$ long-range complexes. As in vacuum, pseudorotation of $I^{ae} \rightarrow I^{ea}X$ in solution is thermodynamically unfavorable (ΔA_{sln} = 4.7 kcal/mol). Solvation is expected to attenuate the strong intramolecular charge–charge interactions that are dominant in vacuum. It decreases the free energy barriers for exocyclic cleavage and P–O ring-opening by 1–2 kcal/mol; that is, the transition state is better solvated than the corresponding intermediate. However, the P–N endocyclic cleavage transition state $TS^{ea}N$ (ΔA_s = −63 kcal/mol) may be less well solvated than the corresponding $I^{ea}N$ intermediate, whose solvation free energy is probably similar to that of the $I^{ee}N/I^{ee}X/I^{ea}X$ intermediates (ΔA_s = −66 to −68 kcal/mol). Thus, $(OH)^-$ attack opposite the ring oxygen of MNP in solution is predicted to yield a mixture of P–O and P–N endocyclic cleavage products as well as exocyclic cleavage products.

4. Discussion

Before discussing the results, the errors that arise from the quantum mechanical and continuum dielectric calculations will be evaluated. The effect of electron correlation on the reaction barriers is indicated by the difference between the HF/3-21+G* and MP2/6-31+G*//HF/3-21+G* activation energies in Figures 2 and 4. This shows that inclusion of electron correlation generally decreases the HF barriers[22] except for the $I^{ee}N \rightarrow TS^{ee}N$ and $I^{ae} \rightarrow TS^{ae}M$ HF activation energies, which are increased by 1 and 0.3 kcal/mol, respectively. The largest effect of electron correlation is observed for the $I^{aa}L \rightarrow TS^{aa}L$ barrier, which decreases from a HF/3-21+G* value of 9.6 to 2.8 kcal/mol at the MP2/6-31+G*//HF/3-21+G* level (Figure 2).

The solvation free energy of $(OH)^-$ is calculated to be −98 kcal/mol, which is in the range of the experimental estimates of 89,[23] −95,[24] −99,[25] and −104[26] kcal/mol. No experimental solvation free energies are available to compare with the calculated values in Table 1. In Figures 3 and 5, the solution barrier associated with two pentacovalent species has a smaller error than that from reactants to the long-range transition state. This is because the electrostatic solvation free energies of pentacovalent endo- and exocyclic cleavage intermediates and transition states as well as rotational transition states are similar (−63 to −72 kcal/mol; see Table 1); thus, the net error in evaluating the solution barrier is likely to be small. Errors arising from the neglect of nonpolar contributions to the solvation free energy difference between pentacovalent species are expected to be even smaller.

In contrast, the solvation free energies of $(OH)^-$, the long-range $TS^{aa}L/TS^{ae}L$ transition state (−78/68 kcal/mol), and neutral MNP (−15 kcal/mol) differ by an order of magnitude. Thus, the absolute errors involved in calculating their electrostatic solvation free energies are also different and do not cancel in evaluating the solution activation free energy from reactants to the long-range transition state. The error in the latter may be compounded by smaller errors due to the neglect of nonpolar contributions. Since inclusion of electron correlation would probably lower the gas-phase barrier and the solvation free energy of the long-range transition states may be underestimated,[14] the computed barrier from reactants to the long-range transition state in solution is likely to be an upper bound.

4.1. Comparison with Experiment: Product Distribution and Stereochemistry. The results presented in section 3 do not support a mechanism that involves amide proton abstraction by the hydroxide ion followed by P–O ring-opening to yield a metaphosphorimidate intermediate (see Scheme 3). Such a mechanism was proposed to explain the basic reactions of 1,3,2-oxazaphospholidines where the nitrogen is unsubstituted.[27] However, the long-range $TS^{ae}L$ transition state does not exhibit significant elongation of the N–H bond even though the hydroxyl ion is in close proximity to the amide group ($O^H–H^N$ = 2.2 Å). The mechanism in Scheme 3 was further tested by abstracting the amide proton in MNP. The resulting species has a $P–O^{ring}$ bond length (1.64 Å) that is 0.14 Å shorter than that in $I^{ae}N$; thus, it is expected to require greater activation free energy for P–O ring-opening compared to $I^{ae}N$.

Figure 3 shows that the rate-limiting step for $(OH)^-$ attack opposite the ring nitrogen of MNP in solution is determined by

(22) Schaefer, H. F. *J. Phys. Chem.* **1985**, *89*, 5336.
(23) Friedman, H. L.; Krishnan, C. V. In *Water: A Comprehensive Treatise*; Franks, F., Ed.; Plenum Press: New York, 1973; Vol. 3, p 1.
(24) Gomer, R.; Tryson, G. *J. Chem. Phys.* **1977**, *66*, 4413.
(25) *CRC Handbook of Chemistry and Physics*; CRC Press: New York, 1985.
(26) Pearson, R. G. *J. Am. Chem. Soc.* **1986**, *108*, 6109.
(27) Hall, C. R.; Inch, T. D.; Williams, N. E. *J. Chem. Soc., Perkin Trans. 1* **1982**, 639–643.

Scheme 3

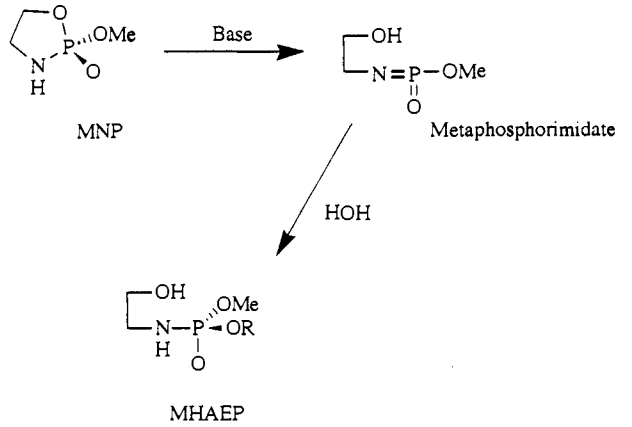

Table 4. Relative Thermodynamic Parameters (kcal/mol) for Rate-Limiting Transition States[a]

	$TS^{ea}H$	$TS^{ae}L$	$TS^{ea}X$	$TS^{ae}N$	TSP
ΔE^b	21.9	22.9	23.6	19.2	22.7
$T\Delta S^c$	1.2	0.8	0.5	1.0	2.3
$\Delta A_{gas}{}^d$	20.7	22.1	23.1	18.2	20.4
$\Delta\Delta A_s{}^e$	−10.3	−10.4	−11.0	−6.0	−7.8
$\Delta A_{sln}{}^f$	10.4	11.7	12.1	12.2	12.6

[a] For $TS^{aa}L \rightarrow X$ where X = $TS^{ea}H$, $TS^{ae}L$, $TS^{ea}X$, $TS^{ae}N$, TSP. [b] $\Delta E = \Delta E_{MP2} + E_{TRV}$. [c] $T\Delta S = [S_{TRV}(X) - S_{TRV}(TS^{aa}L)] \times 298.15^{-3}$. [d] $\Delta A_{gas} = \Delta E - T\Delta S$. [e] $\Delta\Delta A_s = \Delta A_s(X) - \Delta A_s(TS^{aa}L)$. [f] $\Delta A_{sln} = \Delta A_{gas} + \Delta\Delta A_s$.

the long-range transition state $TS^{aa}L$, which is more than 20 kcal/mol higher in free energy than the $TS^{ee}N/TS^{ee}N/TS^{ee}X$ transition states. In contrast, for $(OH)^-$ attack opposite the ring oxygen of MNP in solution (Figure 5) the highest free energy transition state $TS^{ea}H$, is only 1.3, 1.7, 1.8, and 2.2 kcal/mol higher in free energy than the $TS^{ae}L$, $TS^{ea}X$, $TS^{ae}N$, and TSP transition states, respectively. As the differences are within the uncertainty of the present calculations, any or all of these transition states could potentially be rate-limiting. Table 4 shows that the free energy differences between the rate-limiting $TS^{aa}L$ transition state of the $(OH)^-$ + MNP(N) reaction and the $TS^{ea}H$, $TS^{ae}L$, $TS^{ea}X$, $TS^{ae}N$, and TSP transition states of the $(OH)^-$ + MNP(O) reaction share three features: first, the effect of solvation is opposite to the effect in vacuum; second, the magnitude of the gas-phase free energy difference is more than twice the magnitude of the solvation free energy difference; third, the solution free energy of $TS^{aa}L$ is more than 10 kcal/mol greater than that of the transition states along the $(OH)^-$ + MNP(O) pathway. Thus, alkaline hydrolysis of MNP in vacuum and solution is predicted to favor $(OH)^-$ attack opposite the ring oxygen instead of the nitrogen; this is governed by intramolecular electrostatic interactions rather than solvent effects.

The product distribution is determined by the $TS^{ea}H$, $TS^{ea}X$, $TS^{ae}N$, and TSP transition states. As these species are within 2.5 kcal/mol of each other in vacuum and solution, alkaline hydrolysis of MNP is predicted to yield (i) P–O endocyclic cleavage product, the methyl (hydroxyaminoethyl)phosphonate, with inversion of configuration; (ii) P–O exocyclic cleavage products, the aminoethylenephosphonate and methanol, with retention of configuration, and (iii) P–N endocyclic cleavage product, methyl (aminoethyl)phosphate, with retention of configuration (see Scheme 2). The predicted products for the alkaline hydrolysis of MNP in solution are in accord with the observed products for the alkaline hydrolysis of a related system, 2-phenoxy-1,3,2-oxazaphospholidin-2-one (Scheme 4);[28] however, the stereochemistry was not determined, as aqueous basic hydrolysis (R = H in Scheme 4) leads to achiral products.

(28) Cooper, D. B.; Hall, R.; Harrison, J. M.; Inch, T. D. *J. Chem. Soc., Perkin Trans. 1* **1977**, 1969.

Scheme 4

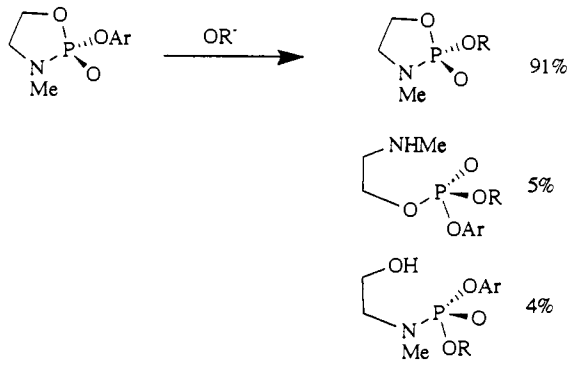

4.2. Ring Strain. Ring strain is qualitatively described here by a comparison of the O–P–X and C–X–P (X = O or N) angles in the cyclic and acyclic phospho-esters. The ring O–P–N (94°), C–O–P (114°), and C–N–P (115°) angles in MNP are smaller than the corresponding HF/3-21+G* angles in the acyclic analogue, which are 109, 126, and 125°, respectively. This indicates ring strain in MNP, which is partially relieved in the distorted TBP long-range transition states, where the differences between the cyclic and acyclic O–P–N or equatorial C–O–P/C–N–P ring angles are smaller than the differences in the ground state.[29] In contrast to the distorted TBP long-range transition states, ring strain is retained in the TBP intermediates.[15] Evidence for the latter is seen in the ring O–P–N angle (83–86°) and the axial C–O–P/C–N–P angle (112–115°), which are less than the corresponding acyclic TBP angles; the equatorial C–O–P/C–N–P angle (119–121°) is similar to its acyclic TBP counterpart[29] and, thus, free of ring strain.

4.3. Apicophilicity. Table 3 shows that both gas-phase and solution free energy differences between the TBP species with an *axial* nitrogen ($TS^{ea}N$, $TS^{ea}H$, $TS^{ea}X$, and $I^{ea}X$) and the corresponding TBP species with an *equatorial* nitrogen ($TS^{ee}N$, $TS^{ee}H$, $TS^{ee}X$, and $I^{ee}X$) are positive (ΔA_{gas} = 5–11 kcal/mol and ΔA_{sln} = 7–11 kcal/mol). The amide group in a TBP prefers to be equatorial rather than axial, as the exocyclic axial oxygen encounters less charge–charge repulsion with an equatorial amide group relative to oxygen and interactions between a equatorial amide proton and an axial oxygen may be more favorable than interactions between an axial amide proton and the equatorial oxygen(s). This is supported by the fact that the equatorial H^N–$O^{5'}$ distances in $TS^{ee}N$, $TS^{ee}H$, $TS^{ee}X$, and $I^{ee}X$ are less than the axial H^N–O^1/O^2 distances in $TS^{ea}N$, $TS^{ea}H$, $TS^{ea}X$, and $I^{ea}X$ (by 0.3–0.8 Å). The P–N bond length is generally longer than the corresponding P–O^{ring} bond (by 0.03–0.05 Å).

In contrast, the solution free energies of $I^{ee}N$, $TS^{ee}H$ and $I^{ee}X$, where the hydroxyl group is equatorial and the methoxy group is axial, are similar (within 2 kcal/mol) to those of $I^{ae}N$, $TS^{ae}M$, and I^{ae}, where the hydroxyl group is axial and the methoxy group is equatorial (Table 3). This suggests that, in these TBP species, the apicophilicity of a hydroxyl group is similar to that of a methoxy group. Note, however, that this in general depends on the other substituents in a TBP. In accord with previous work,[30,31] the equatorial O–H bond is cis to an axial bond in all the TBP intermediates.

4.4. Stereoelectronic Effects. Stereoelectronic effects have often been suggested to control the structure and reactivity of TBP phospho-esters.[32] The physical manifestation of the anomeric effect is thought to be a strengthening of the P–X bond and a weakening of the P–Y bond when the lone pair on atom X is antiperiplanar to a geminal P–Y bond, as illustrated in Scheme

(29) Tole, P.; Lim, C. Manuscript in preparation.
(30) Cramer, C. J. *J. Am. Chem. Soc.* **1990**, *112*, 7965–7972.
(31) Wang, P.; Zhang, Y.; Glaser, R.; Reed, A. E.; Schleyer, P. v. R.; Streitwieser, A. *J. Am. Chem. Soc.* **1991**, *113*, 55–64.
(32) Gorenstein, D. G. *Chem. Rev.* **1987**, *87*, 1047.

Scheme 5

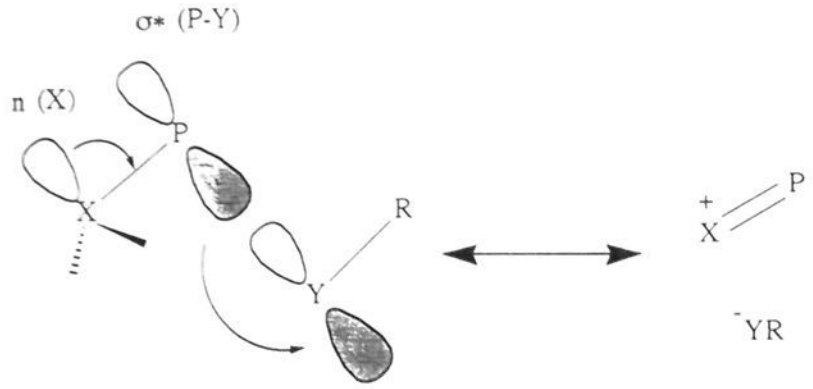

5. The stereoelectronic effect[33] is assumed to derive from the interaction of a doubly occupied molecular orbital (n) with a vacant nondegenerate molecular orbital (σ^*). This leads to a two-electron stabilization energy,

$$\Delta E^{(2)}_{n\sigma^*} = -2\frac{\langle n|\hat{F}|\sigma^*\rangle^2}{\epsilon_n - \epsilon_{\sigma^*}} \qquad (4.2)$$

where $\hat{F}$ is the Fock matrix, which can be obtained from a NBO analysis;[18] the key results are summarized in Table 2.

The NBO analyses of the long-range transition states indicate that the major stabilizing interactions are among the equatorial atoms, especially the lone pairs on O^1 and the antibonding orbital of the equatorial P–X bonds (X = O or N). In comparison, the $\Delta E^{(2)}_{n\sigma^*}$ stabilization energies between the lone pairs (n) on the equatorial methoxy oxygen and the antibonding (σ^*) orbital of the P–O^H bond in the $TS^{aa}L$ and $TS^{ae}L$ long-range transition states are relatively small; thus, stereoelectronic effects do not appear to operate in the long-range transition states. Similarly, the $\Delta E^{(2)}_{n\sigma^*}$ stabilization energies between the lone pairs (n) on the equatorial atoms and the antibonding (σ^*) orbital of the axial bond to be broken in the endo- and exocyclic transition states are small relative to the value in the corresponding rotational transition state (see Table 2). Thus, the NBO analyses do not indicate any stereoelectronic stabilization of the endo- or exocyclic intermediates and transition states.

Furthermore, in the endo- and exocyclic cleavage intermediates and transition states where the amide group is equatorial, the N–H bond is cis to the P–O^{Me} bond so that the nitrogen lone pair is roughly perpendicular to the axial bonds. Although this rules out stereoelectronic effects arising from the lone pair on the equatorial nitrogen, the axial P–$O^{2'}$ bond length in $TS^{ee}N$ (2.47 Å) is greater than that in the corresponding MEP···$(OH)^-$ transition state (2.29 Å), where an electron lone pair on the equatorial ring oxygen is antiperiplanar to the axial P–O^{ring} bond. Thus, the lone pairs on the equatorial ring oxygen do not facilitate ring-opening via stereoelectronic stabilization of the transition state.

4.5. Electrostatic Effects. The long-range electrostatic forces play a crucial role in determining the position and stability of the long-range complexes. The reduced charge–charge repulsion between the exocyclic axial oxygen and the equatorial amide group is partly responsible for the preference of nitrogen to occupy an equatorial position in a TBP (see section 4.3). Intramolecular electrostatic interactions between the hydroxyl group and the departing atom play a dominant role in facilitating endo-/exocyclic cleavage. This is evidenced by the large two-electron stabilization energies of the lone pair on the departing atom and the O–H antibonding orbital (see Table 2) as well as the relatively large positive charge on the polar hydrogens (0.4–0.6e), the negative charge on the departing atom (–1.1 to –1.3e), and the short distance between the two atoms (1.5–2.1 Å) in the endocyclic ($TS^{ee}N$, $TS^{ae}N$, and $TS^{ea}N$) and exocyclic ($TS^{ee}X$ and $TS^{ea}X$) transition states. Further evidence for the role of intramolecular electrostatic interactions in activating ring-opening is provided by the large solution activation free energy difference in the P–O endocyclic cleavage of $I^{ee}N$ (3.9 kcal/mol) and $I^{ae}N$ (13.4 kcal/mol). This is not due to the solution free energy difference between $I^{ee}N$ and $I^{ae}N$ (ΔA_{sln} = –0.1 kcal/mol, Table 3) but to the greater stabilization of the $TS^{ee}N$ transition state relative to the $TS^{ae}N$ transition state (by 9.4 kcal/mol, Table 3); although the methyl hydrogen in the $TS^{ae}N$ transition state is 1.89 Å from the departing oxygen, it has negligible positive charge (0.03e) to stabilize the large negative charge on the departing ring oxygen (–1.16e) in contrast to the $TS^{ee}N$ transition state.

(33) Kirby (1983) has justified the equivalence of using sp^3-hybridized lone-pair orbitals and σ and π orbitals of sp^2-hybridized atoms in discussing anomeric and kinetic anomeric effects.

5. Conclusions

1. Alkaline hydrolysis of MNP in solution is predicted to proceed via $(OH)^-$ attack opposite the ring oxygen instead of the nitrogen. This results in a mixture of P–O endocyclic cleavage product with inversion of configuration and P–O exocyclic and P–N endocyclic cleavage products with retention of configuration.

2. The $(OH)^-$ nucleophile has two important properties: (i) its large solvation free energy (experimentally estimated to be –89 to –104 kcal/mol) induces a barrier for the formation of the long-range transition state in solution (Figure 5); and (ii) the relatively large positive charge on the hydroxyl hydrogen can effectively stabilize the developing negative charge on the departing atom, thus facilitating endo-/exocyclic cleavage.

3. Electrostatic interactions govern the relative stability of the long-range complexes in solution. The reduced charge–charge repulsion between the exocyclic axial oxygen and the face with an equatorial amide group is largely responsible for the preference of nitrogen over oxygen to occupy an equatorial instead of an axial position in a TBP.

4. Ring strain, as manifested by the difference between the O–P–X and C–X–P (X = O or N) cyclic and acyclic angles, does not contribute to the relative stability of the distorted TBP long-range transition states, which are relieved of strain relative the MNP ground state. In contrast, ring strain is retained in the TBP intermediates.

5. Stereoelectronic effects do not control the reaction pathway since there are no apparent interactions between the lone pairs (n) on the equatorial atoms and the antibonding (σ^*) orbital of the axial bond to be broken in the transition states.

Acknowledgment. We are grateful to D. Bashford, M. Sommer, and M. Karplus for the program to solve the Poisson–Boltzmann equation, J. Wiorkewicz and K. Kuczera for the MOLVIB program, and J. Blake for the MINDTOOL program that was employed to draw the ab initio structures.

Supplementary Material Available: Tables of the 3-21+G* bond lengths, bond angles, and dihedral angles (3 pages). This material is contained in many libraries on microfiche, immediately follows this article in the microfilm version of the journal, and can be ordered from the ACS; see any current masthead page for ordering information.